

1 Revisiting the Austral Spring Extratropical Southern
2 Hemisphere zonally assymetric circulation using
3 complex Empirical Orthogonal Functions

4 Elio Campitelli · Leandro B. Díaz ·
5 Carolina Vera ·

6
7 Received: date / Accepted: date

8 **Abstract** abstract

9

10 **Keywords** ·

The research was supported by UBACyT20020170100428BA and the CLIMAX Project funded by Belmont Forum/ANR-15-JCL/-0002-01. Elio Campitelli was supported by a PhD grant from CONICET, Argentina.

Elio Campitelli
Universidad de Buenos Aires, Facultad de Ciencias Exactas y Naturales, Departamento de Ciencias de la Atmósfera y los Océanos. Buenos Aires, Argentina.
CONICET – Universidad de Buenos Aires. Centro de Investigaciones del Mar y la Atmósfera (CIMA). Buenos Aires, Argentina.
CNRS – IRD – CONICET – UBA. Instituto Franco-Argentino para el Estudio del Clima y sus Impactos (IRL 3351 IFAECI). Buenos Aires, Argentina.
E-mail: elio.campitelli@cima.fcen.uba.ar

Leandro B. Díaz
Universidad de Buenos Aires, Facultad de Ciencias Exactas y Naturales, Departamento de Ciencias de la Atmósfera y los Océanos. Buenos Aires, Argentina. CONICET – Universidad de Buenos Aires. Centro de Investigaciones del Mar y la Atmósfera (CIMA). Buenos Aires, Argentina. CNRS – IRD – CONICET – UBA. Instituto Franco-Argentino para el Estudio del Clima y sus Impactos (IRL 3351 IFAECI). Buenos Aires, Argentina.

Carolina Vera
Universidad de Buenos Aires, Facultad de Ciencias Exactas y Naturales, Departamento de Ciencias de la Atmósfera y los Océanos. Buenos Aires, Argentina. CONICET – Universidad de Buenos Aires. Centro de Investigaciones del Mar y la Atmósfera (CIMA). Buenos Aires, Argentina. CNRS – IRD – CONICET – UBA. Instituto Franco-Argentino para el Estudio del Clima y sus Impactos (IRL 3351 IFAECI). Buenos Aires, Argentina.

11 1 Introduction

introduction

12 The large-scale extratropical circulation in the Southern Hemisphere is strongly
 13 zonally symmetric, but its zonal departures are highly relevant for surface im-
 14 pacts and could be related to high-impact climate extremes. Zonal asymme-
 15 tries of extratropical circulation in the Southern Hemisphere strongly modulate
 16 weather systems and regional climate through latitudinal transport of heat,
 17 humidity, and momentum (Trenberth, 1980).

18 One of the main features of the zonally asymmetric circulation are the
 19 Pacific–South American Patterns (Mo and Paegle, 2001), which are associated
 20 with precipitation anomalies in South America, particularly in the September-
 21 October–November trimester (cita). Besides, Raphael (2007) suggests that
 22 variability in the planetary wave 3 projected onto its climatological location
 23 is associated with Antarctic sea ice concentration anomalies. Irving and Sim-
 24 monds (2015) showed that planetary wave amplitude in general is associated
 25 sea ice concentration, as well as temperature and precipitation anomalies.

26 Some of these patterns of variability associated to the zonally asymmet-
 27 ric circulation appear to have experienced secular changes, although to our
 28 knowledge this has not been extensively studied. For instance, Raphael (2003)
 29 found that the amplitude of the zonal wave 1 experienced a large increase and
 30 that the zonal wave 3 experienced changes in its annual cycle between 1958
 31 and 1996.

32 One typical way of describing the zonally asymmetric circulation is by
 33 the amplitude and phase of zonal waves obtained by Fourier decomposition
 34 of geopotential height at each latitude (e.g. van Loon and Jenne, 1972; Tren-
 35 berth, 1980; Turner et al, 2017). This approach suggests that zonal waves 1 and
 36 3 explained most of the variance of the tropospheric extratropical Southern
 37 Hemisphere circulation (van Loon and Jenne (1972)). However, this method-
 38 ology relies on the assumption that the circulation can be meaningfully un-
 39 derstood in terms of zonal waves of constant amplitude along a latitude circle.
 40 This is not valid for meridionally propagating waves or zonal waves with lo-
 41 calised amplitudes. In the case of the wave 3, for example, Trenberth and Mo
 42 (1985) observed that it played a role in blocking events, but this was mostly
 43 due to increased amplitude of a longitudinally localised wave train instead of
 44 an hemispheric-scale zonal wave 3.

45 The fourier technique can be generalised to integrate all planetary wave in-
 46 tensity irregardless of wave number by computing the wave envelope as done
 47 by Irving and Simmonds (2015). This makes it possible to represent plane-
 48 tary waves with different amplitude at different longitudes, but it removes all
 49 information about phase and wave number.

50 Another approach to characterising the Southern Hemisphere circulation is
 51 by using Empirical Orthogonal Functions (EOF, also known as Principal Com-
 52 ponent Analysis). Within the EOF framework, the Southern Annular Mode
 53 (SAM) appears as the leading mode of variability of the tropospheric South-
 54 ern Hemisphere circulation (Fogt and Marshall, 2020) followed by the two
 55 PSA (Mo and Paegle, 2001). The SAM represents a relatively zonally sym-

metric pattern of alternating low pressures in polar latitude and a ring of high pressures in high latitudes with an embedded wave 3 pattern that is more prominent in the Pacific sector. The PSA1 and PSA2 describe the two out-of-phase sides of a meridionally propagating wave train that originates in the Eastern equatorial Pacific and travels towards the South Atlantic following a great-circle arch along the Antarctic Peninsula. These patterns are derived by applying EOF to temporal anomalies, but Raphael (2003) applied EOF methods specifically to zonal anomalies.

EOFs are more flexible than Fourier decomposition modes in the sense that they can capture oscillation patterns that cannot be characterised by purely sinusoidal waves with constant amplitude. Nonetheless, they are restricted to standing oscillation modes and could not represent properly propagating or phase-varying modes such as zonal waves. A single EOF can also represent a mixture of two or more physical modes. The inability of a single EOF to describe travelling waves is what forces the PSA pattern to be described by two EOFs. Irving and Simmonds (2016) characterises this pattern in a Fourier framework. Being a meridionally propagating mode, the PSA cannot be correctly characterised by Fourier decomposition at each latitude circle. As a result, they reprojected meridional wind fields so that the path of the PSA laid on the equator. On this new projection, they could identify the PSA using Fourier decomposition.

Finally, another, hybrid, methodology commonly used consist on identifying particular features of interest and creating indices using simple methods such as averages and differences. The Marshal SAM Index (Marshall, 2003), for example, tries to characterise the SAM by the average difference of sea level pressure between 40°S and 65°S, following Gong and Wang (1999). Raphael (2004) used a similar methodology to describe the wave 3 in the Southern Hemisphere. Instead of using Fourier to compute the amplitude and phase of the zonal wave, they averaged standardised geopotential height anomalies in three points representing the location of the ridges of the zonal wave 3 of the climatological mean. This is equivalent to an index of the amplitude of the zonal wave 3 that projects into the phase of the zonal wave 3 of the mean field. Similarly, Hobbs and Raphael (2010) propose that the zonally asymmetric circulation in the Southern Hemisphere can be described by the strength and location of two anticyclones located in the sub-Antarctic western hemisphere. These methods are grounded on other methods to identify the centres of action for the described phenomena and can be useful to characterise features that are not readily apparent with Fourier or EOF methods. The use of data of only specific regions or locations makes them suitable for easy computation and for extending back into the data-poor past, but also makes them not very robust and unable to capture non-stationary patterns.

Our objective is to improve our understanding of planetary waves in the Southern Hemisphere using an index that is able to capture the phase-varying nature of planetary waves and is flexible enough to describe planetary waves with non-constant amplitude in each latitude circle. We use complex Empirical Orthogonal Functions (Horel, 1984) as a robust extension of EOF analysis that

102 is capable of describing rich structures with meridional and zonal propagation,
 103 and amplitude modulation such as the PSA.

104 We apply this method to characterise the Springtime zonally asymmetric
 105 circulation of the extratropical Southern Hemisphere. To take vertical distri-
 106 bution into account, we analyse both the troposphere and the stratosphere.

107 In Section 2 we describe the methods. In Section 3.1, we analyse the spatial
 108 patterns of each complex EOF. In Section 3.2 we study the spatial regressions
 109 with geopotential height and temperature. In Section 3.3, we analyse the re-
 110 lationship between cEOF1 and Ozone, and between EOF2 and the Southern
 111 Annular Mode and the PSA. In Section 3.4 we look for tropical forcings that
 112 explain the variability of each cEOF. Finally, in Section 3.5 we show the rela-
 113 tionship between these modes of variability and precipitation in South America
 114 and Oceania.

115 2 Data and Methods

116 2.1 Data

We used monthly geopotential height, air temperature, ozone mixing ratio,
 117 and total ozone column (TOC) at 2.5° longitude by 2.5° latitude of hori-
 118 zontal resolution and 37 vertical isobaric levels from the European Centre
 119 for Medium-Range Weather Forecasts Reanalysis version 5 [ERA; Hersbach
 120 et al (2019)] for the period 1979-2019. Most of our analysis was restricted to
 121 the post-satellite era to avoid any confounding factors arising from the in-
 122 corporations of satellite observations, but we also used the preliminary back
 123 extension of ERA5 from 1950 to 1978 (Bell et al, 2020) to look at long-term
 124 trends. Streamfunction was derived from ERA5 vorticity at 200 hPa using the
 125 FORTRAN subroutine FISHPACK (Adams et al, 1999) and horizontal wave
 126 activity fluxes were computed following Plumb (1985). We used Sea Surface
 127 Temperature (SST) monthly fields from Extended Reconstructed Sea Surface
 128 Temperature (ERSST) v5 (Huang et al, 2017) and precipitation monthly data
 129 from the CPC Merged Analysis of Precipitation (Xie and Arkin, 1997), with a
 130 2.5° resolution in latitude and longitude. This rainfall gridded dataset is based
 131 on information from different sources such as rain gauge observations, satellite
 132 inferred estimations and the NCEP-NCAR reanalysis, and it is available since
 133 1979 to present.

135 2.2 Methods

The study is restricted to the spring season, defined as the September-October-
 136 November (SON) trimester. We compute seasonal means for the different vari-
 137 ables, averaging monthly values weighted by the number of days in each month.
 138 We use 200 hPa level to represent the high troposphere and 50 hPa to represent
 139 the lower stratosphere.

141 The amplitude of the zonal waves was obtained through the Fourier trans-
142 form of the spatial field at each latitude circle. We computed the amplitude
143 and phase of the zonal wave 1 by averaging (area-weighted) each variable be-
144 tween 75°S and 45°S for each SON and extracting the wave-1 component of
145 the Fourier spectrum. We chose this latitude band because it is wide enough to
146 capture most of the relevant anomalies for southern hemisphere mid-latitudes.

147 We computed the level-dependent SAM index as the leading EOF of year-
148 round monthly geopotential height anomalies south of 20°S at each level for the
149 whole period according to Baldwin and Thompson (2009). We further split the
150 SAM into its zonally symmetric and zonally asymmetric components (S-SAM
151 and A-SAM indices respectively). These indices were obtained by projecting
152 the zonally asymmetric and zonally symmetric part of the SAM spatial pattern
153 onto monthly geopotential height fields, as proposed by Campitelli et al (2021).
154 Seasonal indices of the Pacific South American patterns (PSA1 and PSA2)
155 were calculated following Mo and Paegle (2001) as the third and fourth leading
156 EOF of seasonal mean anomalies for SH 500 hPa geopotential height combining
157 all seasons. In our study, only the SON values were used.

158 Linear trends were computed by Ordinary Least Squares (OLS) and the
159 95% confidence interval was computed assuming a t-distribution with the ap-
160 propriate residual degrees of freedom (Wilks, 2011).

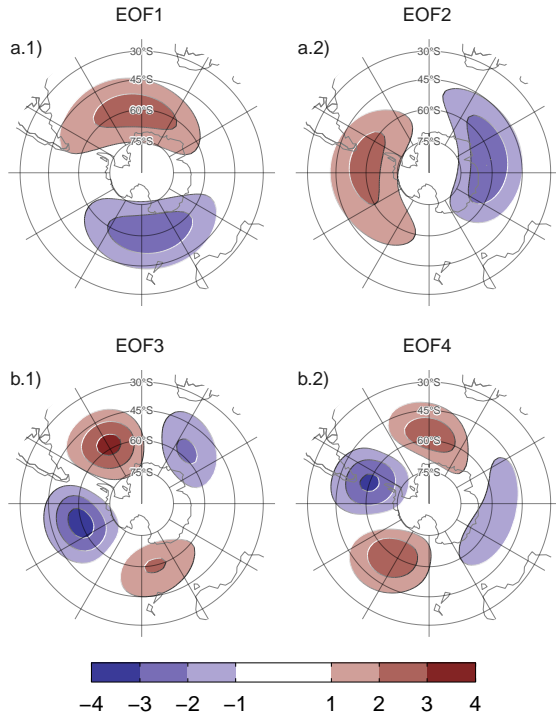
161 2.3 Complex Empirical Orthogonal Functions (cEOF)

complex-empirical-orthogonal-functions-ceof

162 In traditional EOF analysis zonal waves appear as pairs of EOFs, that could be
163 degenerated representing similar patterns but shifted in phase (Horel, 1984).
164 For instance, Figure 1 shows the leading 4 EOFs of SON geopotential height
165 zonal anomalies at 50 hPa south of 20°S. It is clear that the first two EOFs
166 represent the same zonal wave 1 pattern and the last two represent a same
167 zonal wave pattern with shorter wavenumber and four centers of action shifted
168 by 1/4 wavelength. A similar EOF structure can be seen in 200 hPa (not
169 shown). Since each pair of EOFs seem to represent the same phase-varying
170 structure, it would be desirable to combine them into a single index with
171 amplitude and phase.

172 Complex Empirical Orthogonal Functions (cEOF) is a useful method to
173 characterise zonal waves, considering phase-varying structures (Horel, 1984).
174 This method involves computing EOF on the analytic representation of the
175 original field. This representation is a complex field in which the real part is the
176 original variable and the imaginary part is the original data shifted by 90° at
177 each spectral frequency – i.e. its Hilbert transform. The Hilbert transform is
178 usually understood in terms of time-varying signal. However, in this work we
179 apply the Hilbert transform to each latitude circle at each moment in time.
180 Since each latitude circle is a periodic domain, this procedure does not suffer
181 from edge effects.

182 The result of the cEOF methodology is a set of complex spatial patterns
183 and complex time series. The real and imaginary part of each spatial pattern



^{fig:eof-naive}
Fig. 1: Spatial patterns of the leading 4 EOFs of SON zonal anomalies of geopotential height at 50 hPa south of 20°S for the 1979 – 2019 period (arbitrary units).

^{tab:corr-ceof-splitted}
Table 1: Coefficient of determination (R^2) of the absolute magnitude of complex EOFs between 200 hPa and 50 hPa computing EOF separately for each level. p-values lower than 0.01 in bold.

200 hPa	50 hPa		
	cEOF1	cEOF2	cEOF3
cEOF1	0.28	0.01	0.02
cEOF2	0.00	0.60	0.02
cEOF3	0.00	0.00	0.02

¹⁸⁴ represent two phases wave-like spatial patterns that are in quadrature. The
¹⁸⁵ magnitude and argument of each complex time series represent the amplitude
¹⁸⁶ and phase of each zonal wave.

¹⁸⁷ The cEOF methodology is applied to SON geopotential height zonal anomalies
¹⁸⁸ south of 20°S at 50 and 200 hPa, representing a stratospheric and upper
¹⁸⁹ tropospheric level respectively. Table 1 shows the coefficient of determination
¹⁹⁰ between time series of the amplitude of each complex EOF (cEOF) across
¹⁹¹ levels. There's a high degree of correlation between the magnitude of the re-

192 spective cEOF1 and cEOF2 at each level. The spatial patterns of the 50 hPa
193 and 200 hPa cEOFs are also similar (not shown).

194 Both the spatial pattern similarity and the high temporal correlation of
195 cEOFs computed at 50 hPa and 200 hPa suggest that these are, to a large
196 extent, modes of joint variability. This motivates the decision of performing
197 complex EOF jointly between levels. The computation of the cEOFs was car-
198 ried out using data from both levels at the same time, therefore, each cEOF
199 has a spatial component that depends on longitude, latitude and level, and a
200 temporal component that depends only on time.

201 The phase of principal components is defined up to an additive constant.
202 For real principal components, this constant can be either 0 or π , correspond-
203 ing to a change in sign. For complex principal components, it can be any
204 number between 0 and 2π (Horel, 1984). Since any choice is arbitrary and
205 equally valid, we chose the phase of each cEOF so that the real and imaginary
206 parts are aligned with meaningful phases in our analysis. This procedure does
207 not create a spurious correlation, it only takes a known relationship and aligns
208 it with a specific phase. For the first complex principal component, the phase
209 was chosen so that the time series corresponding to the real part has the max-
210 imum correlation with the zonal wave 1 of Total Ozone Column between 75°S
211 and 45°S. This also nearly minimises the correlation with the imaginary part.
212 For the second complex principal component, the phase was chosen so that
213 the coefficient of determination between the Oceanic Niño Index (Bamston
214 et al, 1997) and the real part was minimized, which also nearly maximizes the
215 correlation with the imaginary part.

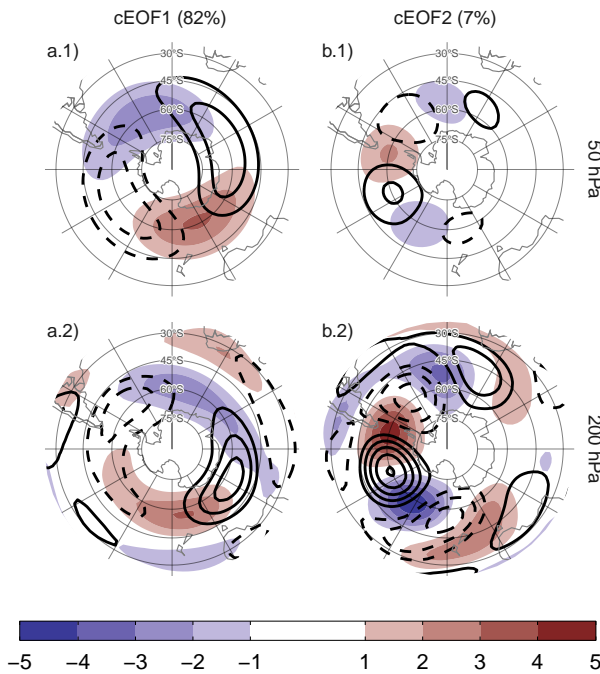
216 While we compute these complex principal components using data from
217 1979 to 2019, we extended the complex time series back to the 1950 – 1978
218 period by projecting monthly geopotential height zonal anomalies standardised
219 by level south of 20°S onto the corresponding spatial patterns.

220 We performed linear regressions to quantify the association between the
221 cEOFs and other variables. For each cEOF, we create regression maps by
222 fitting a multiple linear model involving both the real and the imaginary part.
223 To obtain the linear coefficients of a variable X (geopotential, temperature,
224 precipitation, etc...) with the Imaginary and Real parts of each cEOF we fit
225 the equation

$$X(\lambda, \phi, t) = \alpha(\lambda, \phi) \text{Im(cEOF)} + \beta(\lambda, \phi) \text{Re(cEOF)} + X_0(\lambda, \phi) + \epsilon(\lambda, \phi, t)$$

226 where λ and ϕ are the longitude and latitude, t is the time, α and β are
227 the linear regression coefficients for Imaginary and Real parts respectively, X_0
228 and ϵ are the constant and error terms respectively.

229 We evaluated statistical significance using a two-sided t-test and, in the
230 case of regression maps, p-values were adjusted by controlling for the False
231 Discovery Rate (Benjamini and Hochberg, 1995; Wilks, 2016) to avoid mis-
232 leading results from the high number of regressions (Walker, 1914; Katz and
233 Brown, 1991).



²³⁴ Fig. 2: ^{fig:ceofs-1} Spatial patterns for the two leading cEOFs of SON zonal anomalies of geopotential height at 50 hPa and 200 hPa for the 1979 – 2019 period. The shading (contours) corresponds to real (imaginary) part. Arbitrary units.

²³⁴ 2.4 Computation procedures

computation-procedures

²³⁵ We performed all analysis in this paper using the R programming language
²³⁶ (R Core Team, 2020), using data.table (Dowle and Srinivasan, 2020) and
²³⁷ metR (Campitelli, 2020) packages. All graphics are made using ggplot2 (Wick-
²³⁸ ham, 2009). We downloaded data from reanalysis using the ecmwfr package
²³⁹ (Hufkens, 2020) and indices of the ENSO with the rsoi package (Albers and
²⁴⁰ Campitelli, 2020). The paper was rendered using knitr and rmarkdown (Xie,
²⁴¹ 2015; Allaire et al., 2020).

²⁴² 3 Results

results

²⁴³ 3.1 cEOF spatial patterns

spatial

²⁴⁴ To describe the variability of the circulation zonal anomalies, the spatial and
²⁴⁵ temporal parts of the first two leading cEOFs of zonal anomalies of geopotential
²⁴⁶ height at 50 hPa and 200 hPa, computed jointly at both levels, are shown in
²⁴⁷ Figures 2 and 3. The first mode (cEOF1) explains 82% of the variance, while
²⁴⁸ the second mode (cEOF2) explains a smaller fraction (7%). In the spatial

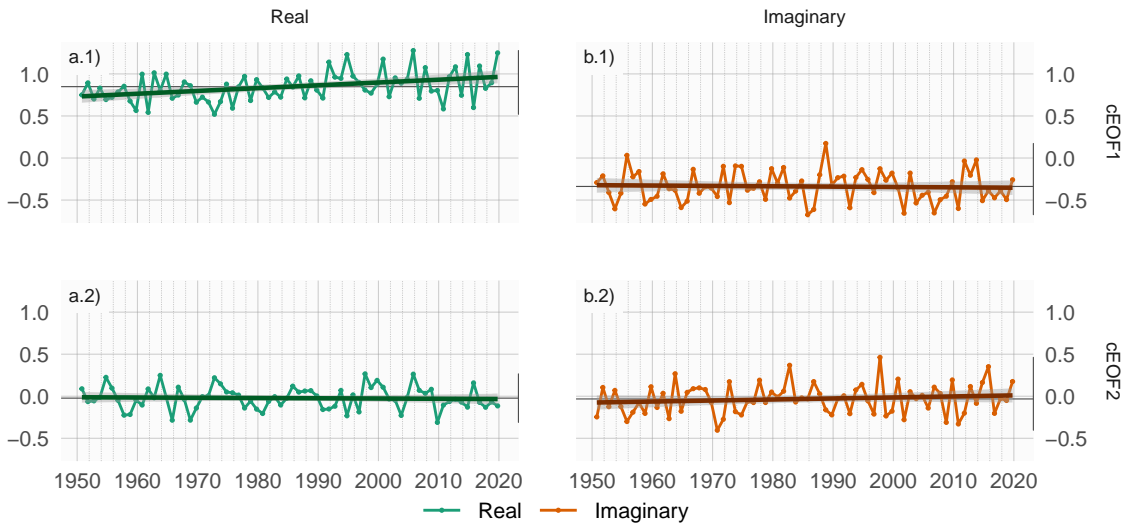


Fig. 3: Time series extended using ERA5 back extended preliminary edition (period 1950 – 1978) and ERA5 (period 1979 – 2019). Dark straight line is the OLS trend. Black horizontal and vertical line mark the mean value and range of each time series respectively.

`fig:extended-series`

249 patterns (Fig. 2), the real and the imaginary components are in quadrature
 250 by construction, so that each cEOF describe a single wave-like pattern whose
 251 amplitude and position (i.e. phase) is controlled by the magnitude and phase
 252 of the temporal cEOF. The wave patterns described by these cEOFs match
 253 the patterns seen in the traditional EOFs of Figure 1.

254 The cEOF1 (Fig. 2 column a) is a hemispheric wave 1 pattern with maxi-
 255 mum amplitude at high latitudes. At 50 hPa the Real cEOF1 has the maximum
 256 of the wave 1 at 150°E and at 200 hPa, the maximum is located at around
 257 175°E indicating a westerly shift in phase. The cEOF2 (Fig. 1 column b) shows
 258 also a zonal wave-like structure with maximum amplitude at high latitudes,
 259 but with shorter spatial scales. In particular, its dominant structure at both
 260 levels is a wave 3 but with larger amplitude in the pacific sector. This modu-
 261 lated amplitude is especially apparent at 200 hPa. There is no apparent phase
 262 shift but the amplitude of the pattern is greatly reduced in the stratosphere,
 263 suggesting that this barotropic mode represents mainly tropospheric variabil-
 264 ity.

265 All cEOFs have non zero mean (Fig. 3) because the geopotential fields that
 266 enter into the cEOFs algorithm are anomalies with respect to the zonal mean
 267 instead of the time mean. However, cEOF2's mean is almost zero, which indi-
 268 cates that only cEOF1 includes variability that significantly projects onto the
 269 mean zonally anomalous field. There are no significant simultaneous correla-
 270 tion between the time series. Both cEOFs show year-to-year variability but
 271 show no evidence of decadal variability.

272 There is only a significant upward trend in the real component of cEOF1
 273 (Fig. 3a.1, p-value < 0.001) and no significant trend in any of the complex
 274 components of cEOF2. The positive trend in the Real cEOF1 translates into
 275 a positive trend in cEOF1 magnitude, but not in the phase (not shown). This
 276 long-term change indicates an increase in the magnitude of the high latitude
 277 zonal wave 1. A similar observation was made by Raphael (2003), who detected
 278 a step after around 1975 in the leading EOF of August-September-October 500
 279 hPa zonal geopotential height anomalies, which is similar to the cEOF1.

280 3.2 cEOFs Regressions

281 The spatial patterns shown in Figure 2 are derived by removing the zonally
 282 symmetric circulation, so they might not include all the variability that is actu-
 283 ally associated with the cEOF time series. To understand the full geopotential
 284 height field changes associated with each cEOF, we computed regression pat-
 285 terns of the full geopotential fields onto each cEOF.

286 Figure 4 shows regression maps of SON geopotential height anomalies upon
 287 cEOF1. At 50 hPa (Figure 4 row a), both the Real and Imaginary cEOF1 are
 288 associated with planetary wave 1 patterns, that are 90° out of phase. Their
 289 phases coincide with the ones shown in Figure 2a.1, with the positive centre
 290 of the Real cEOF1 located towards the dateline, and the one of the Imaginary
 291 cEOF1 located over Eastern Antarctica. However, the Real cEOF1 pattern is
 292 substantially altered by the zonally symmetric circulation. Instead of a clear
 293 wave 1 pattern, the regression pattern can be better described as a monopole
 294 with its centre displaced from the South Pole.

295 The regression patterns for cEOF1 at 200 hPa (Figure 4 row b) are sim-
 296ilarly influenced by the zonally symmetric circulation. It is only possible to
 297 partially distinguish the wave 1 pattern in relation with the Real cEOF1 (Fig-
 298 ure 4b.1). The Imaginary cEOF1 shows a much more zonally symmetrical
 299 pattern resembling the negative SAM phase.

300 With the exception of the Imaginary cEOF1, it is clear that these patterns
 301 are very different than the fully zonally asymmetric versions (Fig. 2), partic-
 302 ularly at 200 hPa. Moreover, only in the stratosphere these patterns actually
 303 show a distinguishable wave 1 pattern shifted in phase by 90°, suggesting that
 304 using the cEOF method is artificially generating a wave structure at 200hPa.
 305 Therefore, the magnitude and phase of the cEOF1 are associated with the
 306 magnitude and phase of a zonal wave only in the stratosphere. While in the
 307 troposphere, they are associated with slightly off-centre monopoles.

308 Figure 5 shows the regression pattern of geopotential height anomalies
 309 upon the cEOF2. Unlike for cEOF1, in this case the regression patterns are
 310 similar to the fully zonally asymmetric patterns from Figure 2. Although there
 311 are some differences (particularly in 50 hPa), the wave trains identified before
 312 are well characterised and patterns associated with the Real cEOF2 are 90°
 313 out of phase with those associated with the Imaginary cEOF2. Zonal wave
 314 3 dominates all fields, but only in the western hemisphere, over the Pacific

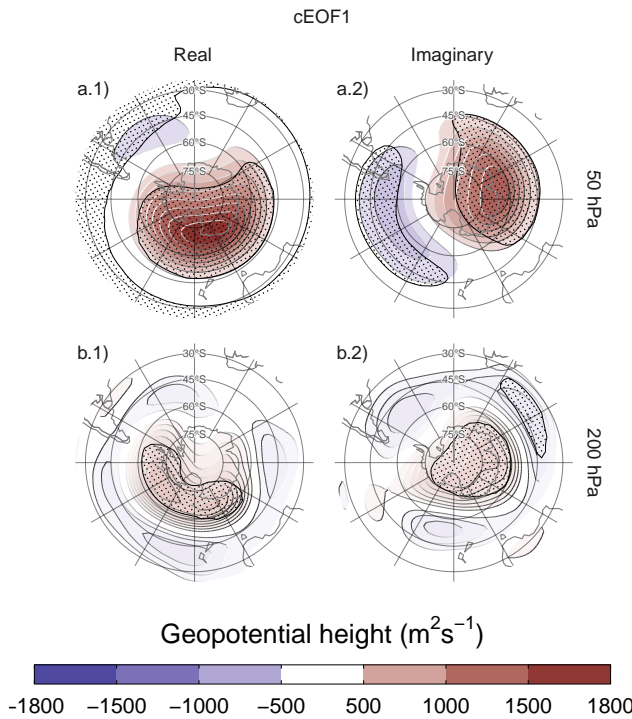


fig: eof1-regr-gh
Fig. 4: Regression of SON geopotential height anomalies ($\text{m}^2 \text{s}^{-1}$) with the (column 1) real and (column 2) imaginary parts of the first cEOF for the 1979 – 2019 period at (row a) 50 hPa and (row b) 200 hPa. These coefficients come from multiple linear regression involving the real and imaginary parts. Areas marked with dots have p-values smaller than 0.01 adjusted for False Detection Rate.

315 and Atlantic Oceans. cEOF2 then represents an equivalent barotropic wave
 316 train that is very similar to the the Pacific South American Patterns (Mo and
 317 Paegle, 2001). Comparing the location of the positive anomaly near 90°W in
 318 column b of Figure 5 with Figures 1.a and b from Mo and Paegle (2001), the
 319 Real cEOF2 can roughly be identified with PSA2, while the Imaginary cEOF2
 320 resembles PSA1.

321 3.3 cEOFs relationship with known modes of variability

other-variables

322 3.3.1 SAM

sam

323 To explore the relationship between SAM and the modes described from the
 324 cEOF, we compute the coefficient of determination between the cEOFs time-
 325 series and the three SAM indices (SAM, A-SAM and S-SAM) at each ver-

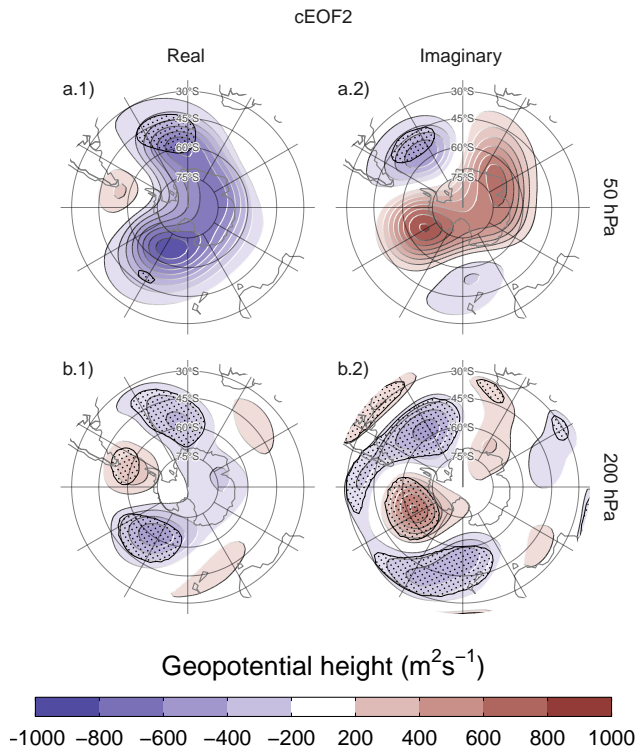


Fig. 5: Same as Figure 4 but for the second cEOF.
fig:eof2-regr-gh

tical level (Fig. 6). The SAM index is statistically significant correlated with the Real cEOF1 in all levels, and with the Imaginary cEOF1 and Imaginary cEOF2 in the troposphere. Correlations between SAM and the Real cEOF2 are non-significant.

The relationship between the tropospheric SAM and cEOF1 is explained entirely by the zonally symmetric component of the SAM as shown by the low and statistically non-significant correlations between the A-SAM and either the Real or Imaginary cEOF1 and the high correlation with the S-SAM below 100 hPa. In the stratosphere, the Real cEOF1 is correlated with both A-SAM and S-SAM, while the Imaginary cEOF1 is highly correlated only with the A-SAM. These correlations are consistent with the regression patterns of geopotential height in Figure 4 and their comparison with those obtained for SAM, A-SAM and S-SAM by Campitelli et al (2021).

In the case of cEOF2, the moderate correlation between SAM and Imaginary cEOF2 becomes extremely high only when the zonally asymmetric variability of the SAM is considered. The Imaginary cEOF2 explains up to 92% of A-SAM variance, reached the maximum value at 225 hPa (Figure 6.b2). Such extremely high correlation between the asymmetric SAM and the Imaginary

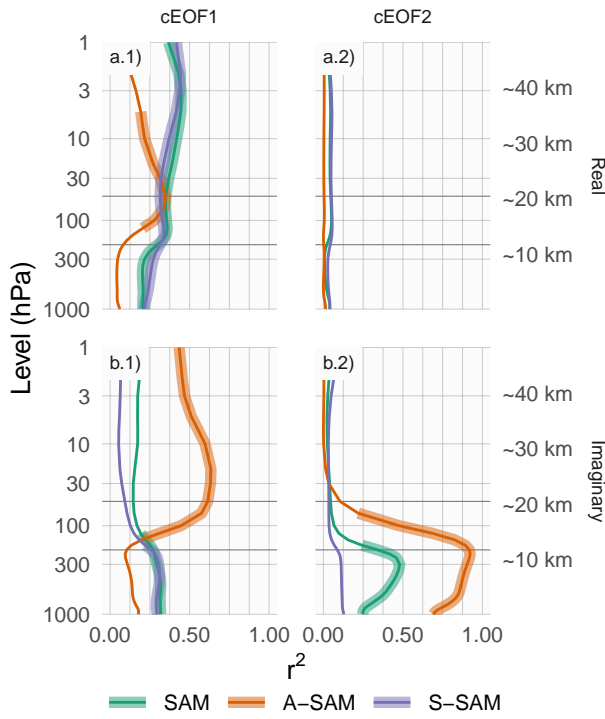


Fig. 6: ^{fig:sam-eof-vertical} Coefficient of determination between the real and imaginary part of each cEOF and the SAM, Asymmetric SAM (A-SAM) and Symmetric SAM (S-SAM) indices computed at each level according to Campitelli et al (2021) for the 1979 – 2019 period. Thick lines represent estimates with p-value < 0.01 corrected for False Detection Rate (Benjamini and Hochberg, 1995).

Table 2: ^{tab:psa-eof2} Correlations between the Real and Imaginary parts of cEOF2 and the PSA1 and PSA2 modes computed as the second and third EOFs of seasonal geopotential height anomalies (following Mo and Paegle, 2001) for the 1979 – 2019 period. 95% confidence intervals in parenthesis. p-values lower than 0.01 in bold.

PC	cEOF2	
	Real	Imaginary
PSA1	-0.32 (CI: -0.57 – -0.02)	-0.82 (CI: -0.9 – -0.69)
PSA2	0.81 (CI: 0.67 – 0.9)	-0.06 (CI: -0.36 – 0.25)

³⁴⁴ cEOF2 suggests that these might be different ways of characterising the same
³⁴⁵ phenomenon.

346 *3.3.2 PSA*

psa

347 Due to the similarity between the PSA patterns and the cEOF2 spatial pat-
 348 terns (Fig. 5), we study the relationship between these modes. Table 2 shows
 349 the correlations between the two PSA indices and the timeseries for Real and
 350 Imaginary phase of cEOF2. As anticipated by Figure 5, there is a strong cor-
 351 relation between PSA1 and Imaginary cEOF2, and between PSA2 and Real
 352 cEOF2. Conversely, there is no relationship between PSA1 and Real cEOF2,
 353 and between PSA2 and Imaginary cEOF2. As a result, cEOF2 represents well
 354 both the spatial structure and temporal evolution of the PSA modes, as well
 355 as it is possible to make a rather clean association between its two phases
 356 and the two PSA modes. So, It could be concluded that the same particular
 357 rotation of cEOF2 that maximises the association between cEOF2 parts and
 358 PSA modes, is the one which maximises the relationship between ENSO and
 359 Imaginary cEOF2.

360 The reason the conventional EOF analysis arrives at the same separation
 361 than our particular cEOF rotation is probably the fact that not all phases are
 362 equally frequent. To visualize that, Figure 7 shows an histogram that counts
 363 the number of SON years in which the cEOF2 was close to each of the four
 364 particular phases (positive/negative Real/Imaginary), with the observations
 365 for each season marked as rugs on the horizontal axis. For instance, years
 366 with cEOF2 phase within 45° of 0° are nearest the “positive Real” phase.
 367 About two thirds of time cEOF2 has a phase similar to either the negative
 368 or positive Imaginary phase. It could be seen that Imaginary phase is the
 369 most common phase and It is also, by construction, the direction that has the
 370 maximum relationship with ENSO. Therefore, the Imaginary cEOF2 explains
 371 more variance than the Real cEOF2 and conventional EOF analysis will tend
 372 to separate the two.

373 The result obtained here is similar to the one obtained by Irving and Sim-
 374 monds (2016). They show that the phase distribution of the PSA-like variabil-
 375 ity obtained by them is bimodal and isolate the PSA pattern from the rest
 376 of the PSA-like variability by selecting events that are near the peaks of the
 377 distribution (compare our Figure 7 with their Figure 6).

378 The advantage of our method is that it is much simpler to implement,
 379 it provides magnitude and phase naturally, and it facilitates the description
 380 of this mode as a propagating wave instead of as standing oscillations. As a
 381 consequence, the cEOF2 offers an alternative way of representing the PSA
 382 which has several advantages over using the second and third EOFs.

383 *3.3.3 Temperature and Ozone*

temperature-and-ozone

384 The relation between cEOFs and air temperature was also evaluated. Fig-
 385 ure 8 shows regression patterns of air temperature at 50hPa and 200hPa onto
 386 cEOF1. In both levels, the Real cEOF1 is associated with a positive monopole
 387 over the South Pole with its centre moved slightly towards 150°E (Fig. 8 col-
 388 umn 1). On the other hand, the regression maps on the Imaginary cEOF1

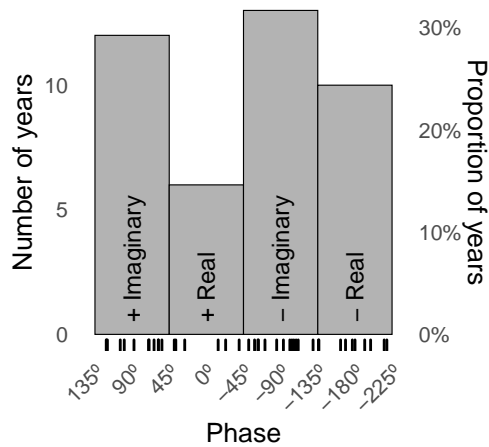


Fig. 7: `fig:phase-histogram` Histogram of phase distribution of cEOF2 for the 1979 – 2019 period. Bins are centred at 90° , 0° , -90° , -180° with a binwidth of 90° . The small vertical lines near the horizontal axis mark the observations.

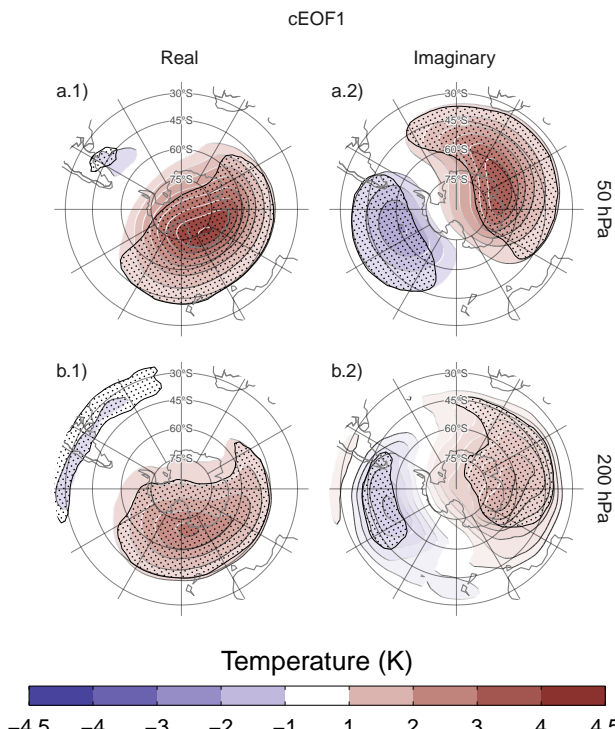


Fig. 8: `fig:EOF1-regr-t` Same as Figure 4 but for air temperature (K).

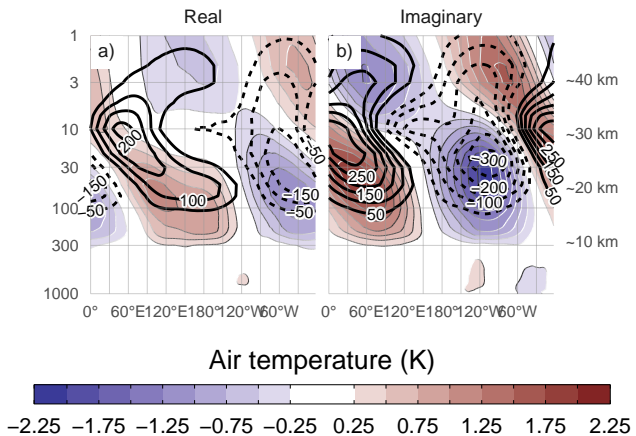


Fig. 9: Regression of SON anomalies of mean air temperature (shaded, Kelvin) and ozone mixing ratio (contours, negative contours with dashed lines, labels in parts per billion by mass) averaged between 75°S and 45°S with the (a) real and (b) imaginary parts of the first cEOF for the 1979 – 2019 period.

389 show a more clear wave 1 pattern with its maximum around 60°E. The distribution
 390 of temperature regression coefficients at 50 hPa and at 200 hPa mirror
 391 the geopotential height regression maps at 50 hPa (Fig. 4).

392 Figure 9 shows the vertical distribution of the regression coefficients on
 393 cEOF1 from zonal anomalies of air temperature and zonal anomalies of ozone
 394 mixing ratio averaged between 75°S and 45°S. Temperature zonal anomalies
 395 associated with cEOF1 show a clear wave 1 pattern for both real and imaginary
 396 components throughout the atmosphere above 250 hPa with a change in sign
 397 above 10 hPa. Following hydrostatic balance, this is the level in which the
 398 geopotential anomaly have maximum amplitude (not shown).

399 The maximum ozone anomalies are co-located with the minimum temperature
 400 anomalies above 10 hPa and with the maximum temperature anomalies
 401 below 10 hPa (Fig. 9). Therefore, the ozone zonal wave 1 is anticorrelated
 402 with the temperature zonal wave 1 in the upper stratosphere, and directly
 403 correlated in the upper stratosphere. This change in phase is observed in
 404 ozone anomalies forced by planetary waves that reach the stratosphere. In
 405 the photochemically-dominated upper stratosphere, cold temperatures inhibit
 406 the destruction of ozone. On the other hand, in the advectively-dominated
 407 lower stratosphere, ozone anomalies are 90° out of phase with horizontal and
 408 vertical transport, which are in addition 90° out of phase with temperature
 409 anomalies (Hartmann and Garcia, 1979; Wirth, 1993; Smith, 1995).

410 The regression maps of cEOF1 with fields of Total Ozone Column (TOC)
 411 (Fig. 10) show zonal wave 1 patterns in TOC associated with both phases of
 412 cEOF1. Climatologically, the springtime Ozone minimum is located off the
 413 South Pole and towards the Weddell Sea (Grytsai, 2011). Thus, the Real
 414 cEOF1 regression pattern (Figure 10a) coincides with the climatological po-

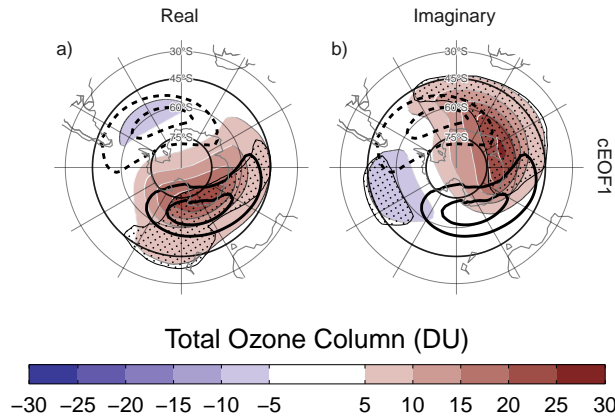


Fig. 10: `fig:o3-regr` of SON mean Total Ozone Column anomalies (shaded, Dobson Units) with the (a) real and (b) imaginary parts of the cEOF1 for the 1979 – 2019 period. On contours, the mean zonal anomaly of Total Ozone Column (negative contours in dashed lines, Dobson Units). Areas marked with dots have p-values smaller than 0.01 adjusted for False Detection Rate.

415 sition of the ozone hole while the one for the Imaginary cEOF1 is shifted by
416 90°.

417 There is a close spatial relationship between amplitudes and phases of the
418 cEOF1 and TOC planetary wave 1 between 75°S and 45°S. The correlation
419 between the amplitude of both indices is 0.77 (CI: 0.61 – 0.87) and 0.49 (CI:
420 0.21 – 0.69) between their phases.

421 3.4 Tropical sources

422 The connections between cEOFs and Tropical sources are also assessed. Fig-
423 ure 11 shows the regression maps of Sea Surface Temperatures (SST) and
424 Streamfunction anomalies at 200 hPa respectively upon cEOF2. The Imagi-
425 nary cEOF2 is associated with strong positive SST anomalies on the Central
426 Pacific and negative anomalies over an area across the North of Australia and
427 New Zealand, the South Pacific Convergence Zone (SPCZ) (Figure 11.a2).
428 This pattern is almost canonically positive ENSO (Bamston et al, 1997) and
429 indeed, the correlation between the Imaginary cEOF2 and the Oceanic Niño
430 Index (Bamston et al, 1997) is significant and very high 0.76 (CI: 0.59 – 0.87).
431 Besides, the Imaginary cEOF2 is associated with strong wave-like streamfunc-
432 tion anomalies emanating from the tropics (Figure 11.b2). This is consistent
433 with the effect of ENSO on the extratropics: SST anomalies initiate anomalous
434 tropical convection that excites Rossby waves that propagate meridionally
435 towards higher latitudes (Mo, 2000).

436 Since the Real cEOF2 represents just a different phase of the same wave
437 train, it would be expected to show a similar forcing pattern to the Imaginary

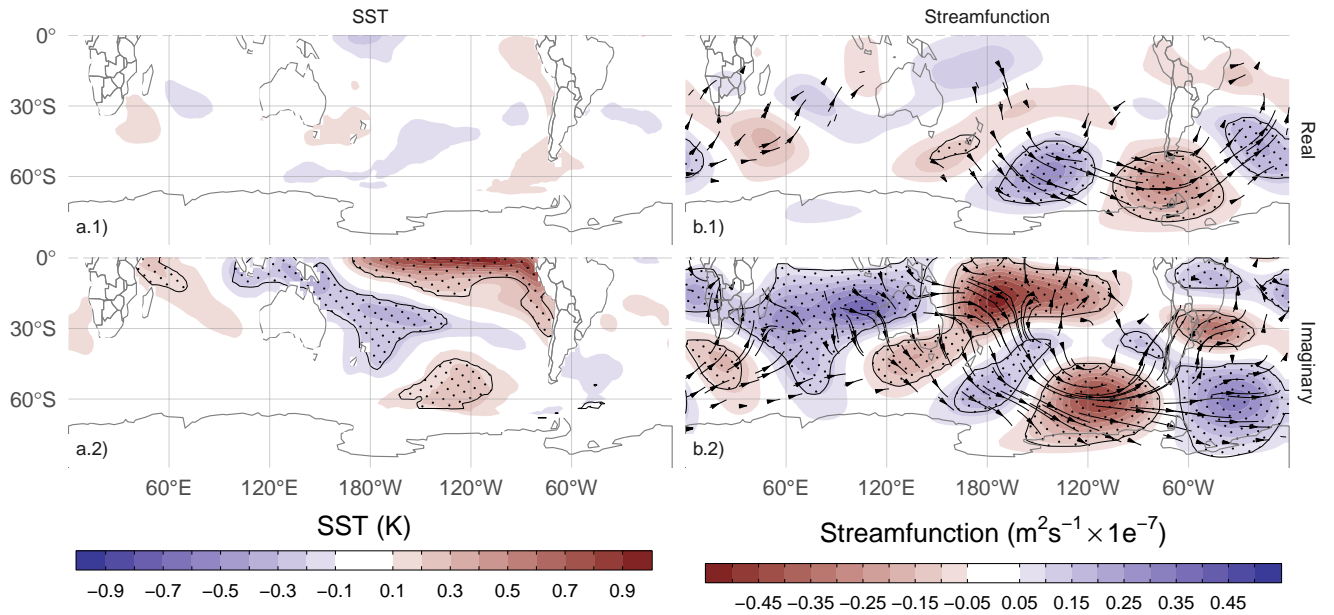


Fig. 11: Regression maps of cEOF2 with SST (K, column a) and streamfunction zonal anomalies ($m^2/s \times 10^{-7}$, shaded) with their corresponding activity wave flux (vectors) (column b) for the 1979 – 2019 period. Areas marked with dots have p-values smaller than 0.01 adjusted for FDR.

`fig:sst-psi-2`

438 cEOF2 with a slight translation of its location. However, Figure 11.a1 and b1
 439 show that the Real cEOF2 is not associated either with any significant SST
 440 nor streamfunction anomalies in the tropics. The correlation between the Real
 441 cEOF2 and ENSO is also not significant (0 (CI: -0.31 – 0.31)). This lack of
 442 tropical signal suggest that the Real cEOF2 and the Imaginary cEOF2 have
 443 very different sources of variability.

444 To better explore the relationship between tropical forcing and phase of the
 445 cEOF2, Figure 12 shows the ONI index against the cEOF2 phase for each SON
 446 trimester between 1979 and 2019, highlighting years in which the magnitude
 447 of cEOF2 is above the median. In years with positive ONI, the phase of the
 448 cEOF2 is mostly around $+90^\circ$ (corresponding with positive imaginary part)
 449 and vice versa. In years with near neutral ENSO, the phase of the cEOF2
 450 is much more variable. The black line in Figure 12 is a sinusoidal fit of the
 451 relationship between ONI and cEOF2 phase. The r^2 corresponding to the fit is
 452 0.56, statistically significant with $p\text{-value} < 0.001$, indicating a quasi-sinusoidal
 453 relation between these two variables.

454 Furthermore, Figure 12 suggest that highest amplitude cEOF2 years tend
 455 to coincide with strong ENSO years. The correlation between the absolute
 456 magnitude of the ONI and the magnitude of the cEOF2 is 0.45 (CI: 0.17
 457 – 0.67). This relationship, however, appears to be driven only by the three

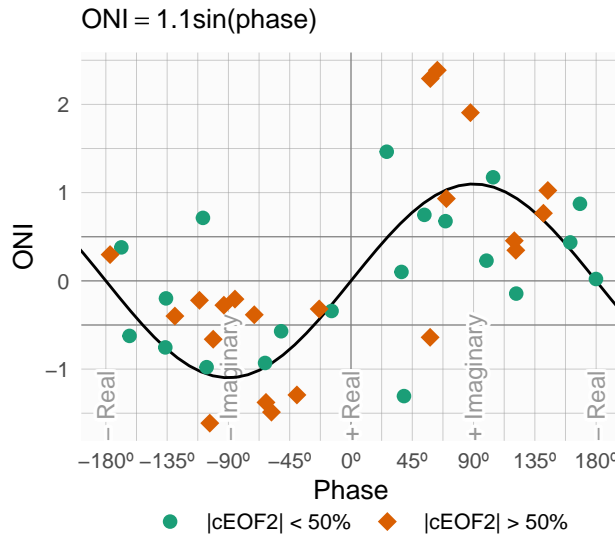


Fig. 12: `fig:enso-phase`
ONI plotted against cEOF2 phase for the 1979 – 2019 period. Years with magnitude of cEOF2 greater or smaller than the 50th percentile are shown as orange circles and green diamonds respectively. Black line is the fit $\text{ONI} \sim \sin(\text{phase})$ computed by weighted OLS using the magnitude of the cEOF2 as weights.

years with strongest ENSO events in the period (2015, 1997, and 1982) which also coincide with the three years with strongest cEOF2 magnitude. If those years are removed, the correlation becomes non-significant (0.05 (CI: -0.28 – 0.36)). Furthermore, even when using all the datapoints, the Spearman correlation –which is robust to outliers– is also non-significant (0.2, p-value= 0.21). Therefore, the relationship between the magnitude of the cEOF2 train wave and ONI remains uncertain.

It could be concluded that the wave train represented by cEOF2 can be both part of the internal variability of the extratropical atmosphere or forced by tropical SSTs. In the former case, the wave train has little phase preference. However, when cEOF2 is excited by tropical SST variability, it tends to remain locked to the imaginary phase. This explains the relative overabundance of years with cEOF2 near positive and negative imaginary phase in Figure 7.

Figure 13 shows SST and streamfunction regression maps for cEOF1. Unlike the cEOF2 case, there is no significant pattern of SST anomalies associated with either the Real or Imaginary cEOF1. Consistently, streamfunction anomalies do not show any tropical influence. Instead, the real and Imaginary cEOF1 are associated with zonally wave activity fluxes in the extra-tropics around 60°S, except for an equatorward flow from the coast of Antarctica around 150°E in the real component. This suggests that its variability is driven primarily by the internal variability of the extra-tropics.

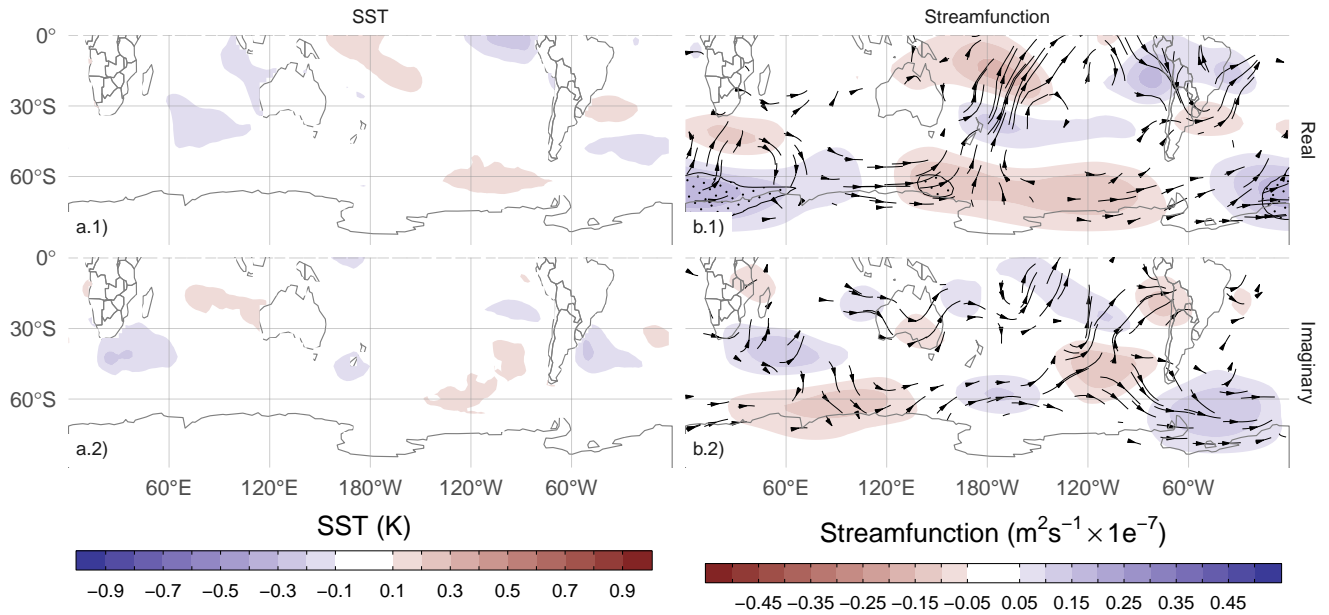


Fig. 13: Same as Figure 11 but for cEOF1.

fig:sst-psi-1

479 3.5 Precipitation

480 The influence of cEOFs variability in continental rainfall of extra-tropical
 481 Southern Hemisphere is also explored. We focus on South America and Oceania
 482 sectors because there are no relevant signals in southern Africa (not shown).

483 The precipitation anomalies in Oceania associated with cEOF1 are weak
 484 and not statistically significant (Figure 14 column 1) whereas cEOF2 is associ-
 485 ated with large and widespread anomalies. The Real cEOF2 is associated with
 486 positive seasonal anomalies in Northern and Eastern Australia, and negative
 487 ones over New Zealand, while precipitation anomalies associated with Imag-
 488 inary cEOF2 are negative over all Eastern Australia. As it could be expected,
 489 these negative anomalies are similar to the springtime precipitation anomalies
 490 observed in relation with the Asymmetric SAM (Campitelli et al, 2021) and
 491 ENSO (Cai et al, 2011). **Acá te faltaría sacar un poco más el jugo asociando**
 492 **con la figura 11. Además, ¿revisaste si podes también usar algún resultado**
 493 **asociado a los PSA?**

494 To better understand the relationship between precipitation anomalies over
 495 Eastern Australia and the cEOF2, Figure 15 plots precipitation anomalies av-
 496 eraged over Eastern Australia (box in Figure 14) as a function of cEOF2 phase.
 497 The black line shows a sinusoidal fit, whose coefficients are fitted by weighted
 498 least squares using the magnitude of the EFO2 as weight. The r^2 correspond-
 499 ing to the fit is 0.41 (p-value < 0.001). There is a strong relationship between
 500 the phase of the cEOF2 and precipitation anomalies in Eastern Australia, but

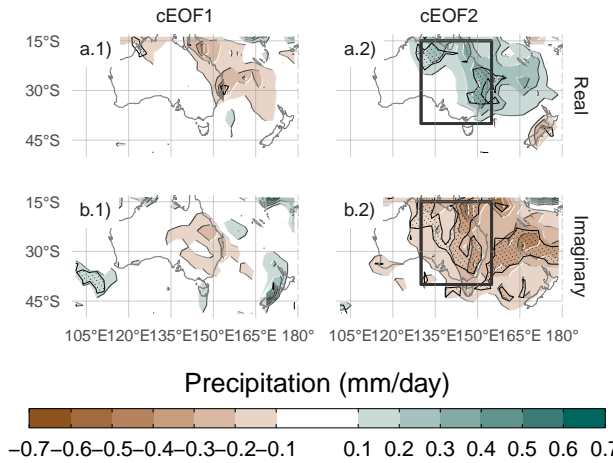


Fig. 14: [fig:pp-oceania](#) Regression of SON mean precipitation anomalies in Oceania (mm per day, shaded) with the (row a) real and (row b) imaginary pars of the (column 1) cEOF1 and (column 2) cEOF2. For the 1979 – 2019. Areas marked with dots have p-values smaller than 0.01 adjusted for False Detection Rate. In black is the West Australia region, defined as the box between 130°E and 155°E and 40°S and 15°S.

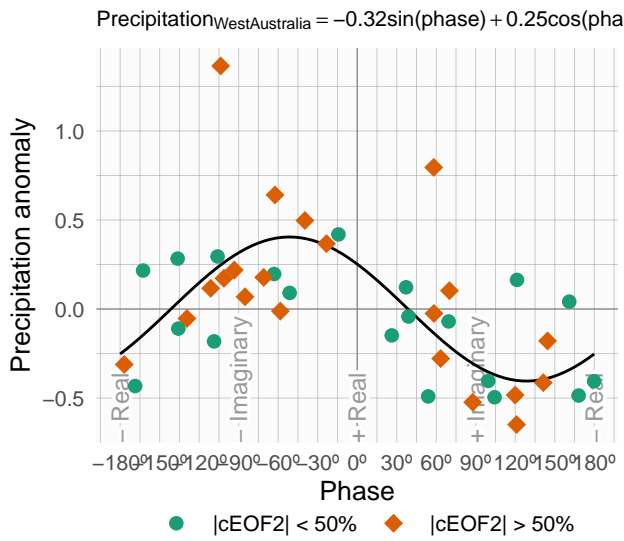


Fig. 15: [fig:australia-pp-phase](#) Same as Figure 12 but for precipitation anomalies averaged between 130°E and 155°E and 40°S and 15°S (box shown in Figure 14 column b) in $\frac{\text{mm}}{\text{day}}$. Black line is the fit precipitation $\sim \sin(\text{phase}) + \cos(\text{phase})$ computed by weighted OLS using the magnitude of the cEOF2 as weights.

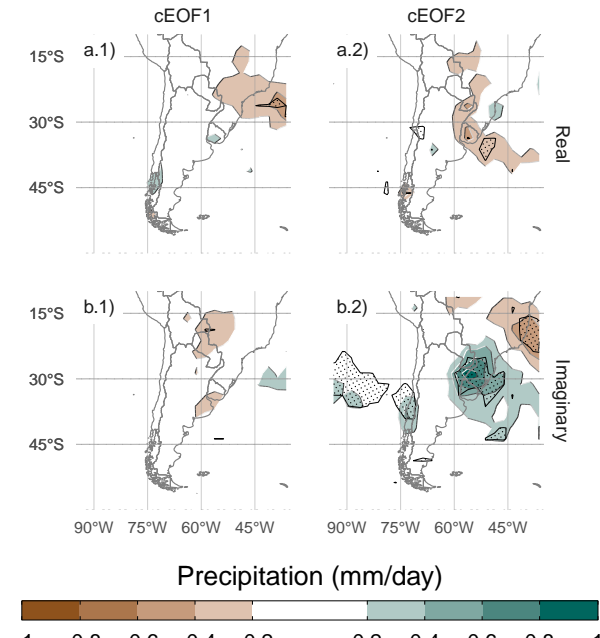


Fig. 16: ^{fig:pp-americas} As Figure 14 but for South America

501 the Real and Imaginary phases we chose are not exactly aligned with the direction
 502 that maximises this relationship. To perform a more in-depth analysis of
 503 the relationship between this pattern and precipitation in this region, it would
 504 be recommended to align one of the axis (either the Real or the Imaginary)
 505 to the phase that maximises the described relationship.

506 Figure 16 shows regression maps of seasonal precipitation with each cEOF
 507 in South America. cEOF1 is associated with negative regressions coefficients
 508 for precipitation in Southern Brazil and Paraguay, although these are not
 509 statistically significant (Fig. 16 column 1). The strongest precipitation re-
 510 gression coefficients are the ones associated with the Imaginary cEOF2. The
 511 positive regression coefficients on Southeastern South America (SESA) and
 512 Central Chile, and negative ones over South Atlantic Convergence Zone is
 513 a well-known springtime precipitation signature of ENSO (Cai et al., 2020)
 514 and it is also similar to the precipitation anomalies associated with the A-
 515 SAM (Campitelli et al., 2021). *Lo mismo que te puse antes. Te faltaría sacar*
 516 *un poco más el jugo asociando con la figura 11. Además, ¿revisaste si puedes*
 517 *también usar algún resultado asociado a los PSA?*

518 This is not surprising considering the close relationship between the ONI,
 519 the A-SAM index and the Imaginary cEOF2 shown previously, but further
 520 consolidates the identification of this mode with the PSA pattern. On the other
 521 hand, the Real cEOF2 is associated with negative precipitation anomalies
 522 in a smaller area of SESA. Resembling the relationship between ONI and

523 the phase of cEOF2 (Fig. 12), there is a cEOF2 phase dependence of the
524 precipitation anomalies in SESA (not shown). These variables could be related
525 wth a significant sinusoidal fit that has a statistically significant coefficient of
526 determination of 0.27.

527 4 Conclusions

528 In this study we assessed the Austral Spring Extratropical Southern Hemisphere
529 zonally assymetric circulation. For this purpose, two complex indices
530 were derived using Complex Empirical Orthogonal Functions. This allowed
531 us to characterise both the amplitude and phase of planetary waves that are
532 not perfectly organised as sinusoidal waves with constant amplitude at each
533 latitude circle.

534 The first complex EOF represents the variability of the zonal wave 1 in
535 the stratosphere, but represents a more zonally symmetric monopole in the
536 troposphere. There is a statistically positive trend in the magnitude of this
537 cEOF, which is consistent with previous studies that showed secular changes
538 in springtime wave-1-like patterns (e.g. Raphael, 2003). This mode is closely
539 related to stratospheric variability such as anomalies in Total Ozone Column.
540 Otherwise, this complex EOF is not related with SST variability and continental
541 precipitation in the Southern Hemisphere.

542 The second complex EOF represents a wave-3 pattern with maximum magnitude
543 in the Pacific sector. Essentially, it is an alternate representation of the
544 PSA1 and PSA2 patterns (Mo and Paegle, 2001). We show that the Imaginary
545 cEOF2 can be identified with the PSA1 and the Real cEOF2 with the
546 PSA2. This cEOF prefers a phase aligned with the Imaginary cEOF2, because
547 when ENSO is active, it forces the cEOF2 to be in the Imaginary phase. When
548 ENSO is neutral, the cEOF2 is still active, but with no particular preferred
549 phase. This mirrors the results of Cai and Watterson (2002), who showed that
550 the CSIRO Model can create PSA-like variability even in the absence of ENSO
551 forcing (with a climatological run), but the variability of one of the PSA modes
552 was enhanced when adding the ENSO signal. The magnitude of the cEOF2
553 appears not to be related to the magnitude of ENSO, except frot the three
554 strongest ENSO events in the period which coincide with the three strongest
555 cEOF2 years.

556 We further show that the Imaginary cEOF2 is closely related to the Southern
557 Annular Mode in the troposphere. In fact, it has a very close resemblance
558 to the zonally asymmetric portion of the SAM. This raises the possibility that
559 the asymmetric component of the SAM is actually a statistical contamination
560 of the PSA mode.

561 Precipitation anomalies in South America associated with the Imaginary
562 cEOF2 show a clear ENSO-like impact, with positive anomalies in South-
563 Eastern South America, negative anomalies in Southern Brazil and positive
564 anomalies in central Chile. Precipitation anomalies associated with the Real
565 cEOF2 are low and not statistically significant, showing that the Imaginary

566 phase is optimally aligned with the direction of maximum precipitation
 567 impacts.

568 On the other hand, over Australia, both the Real and Imaginary phase are
 569 associated with significant precipitation anomalies, and we further show that
 570 the direction of maximum impact is not aligned with our chosen rotation of
 571 cEOF2. However, this underscores the benefit of using complex EOF, since it
 572 would be trivial to rotate it. That is, look for the rotation of complex EOF
 573 that maximises the relationship and use that as the relevant index for study
 574 or forecast.

575 To the extent that the cEOF2 can be identified with the PSA, what is the
 576 advantage of the technique proposed here? The spatial fields that the cEOF2
 577 index describes are in quadrature by construction, which makes it possible to
 578 derive a proper amplitude and phase. Furthermore, because of the way they
 579 are constructed, they are not forced to be orthogonal to the SAM. This makes
 580 it possible to study their relationship with the SAM free of the statistical
 581 contamination that comes with the usual definition of the PSA as the second
 582 and third EOFs.

583 Further work should extend this analysis to other seasons and further study
 584 the relationship between the cEOF2 and the SAM. In particular, it is not
 585 clear whether the close identification between the Imaginary cEOF2 and the
 586 Asymmetric SAM arises from physical processes or statistical contamination.

587 Code availability

`code-availability`

588 A version-controlled repository of the code used to create this analysis, includ-
 589 ing the code used to download the data can be found at <https://github.com/>
 590 `eliocamp/shceof`.

591 5 References

`references`

592 References

- 593 Adams JC, Swartztrauber PN, Sweet R (1999) FISHPACK, a package of Fortran
 594 subprograms for the solution of separable elliptic partial differential
 595 equations. <https://www2.cisl.ucar.edu/resources/legacy/fishpack>
- 596 Albers S, Campitelli E (2020) Rsoi: Import Various Northern and Southern
 597 Hemisphere Climate Indices
- 598 Allaire JJ, Xie [aut Y, cre, McPherson J, Luraschi J, Ushey K, Atkins A, Wick-
 599 ham H, Cheng J, Chang W, Iannone R, Dunning A, filter) AYNsL, Schloerke
 600 B, Dervieux C, Aust F, Allen J, Seo J, Barrett M, Hyndman R, Lesur R,
 601 Storey R, Arslan R, Oller S, RStudio, PBC, library) jFj, library; authors
 602 listed in inst/rmd/h/jquery-AUTHORStxt) jcj, library; authors listed in
 603 inst/rmd/h/jqueryui-AUTHORStxt) jUcjU, library) MOB, library) JTB,
 604 library) BcB, Twitter, library) IB, library) AFh, js library) SJR, js library)

- 605 ISh, library) GFt, templates) JMP, Google, library) Ii, library) DRs, li-
606 brary) Ws, Gandy (Font-Awesome) D, Sperry (Ionicons) B, (Ionicons) D,
607 StickyTabs) ALj, filter) BPJpL, filter) AKpL (2020) Rmarkdown: Dynamic
608 Documents for R
- 609 Baldwin MP, Thompson DWJ (2009) A critical comparison of stratosphere–
610 troposphere coupling indices. *Quarterly Journal of the Royal Meteorological
611 Society* 135(644):1661–1672, DOI 10.1002/qj.479
- 612 Bamston AG, Chelliah M, Goldenberg SB (1997) Documentation of a
613 highly ENSO-related sst region in the equatorial pacific: Research note.
614 *Atmosphere-Ocean* 35(3):367–383, DOI 10.1080/07055900.1997.9649597
- 615 Bell B, Hersbach H, Berrisford P, Dahlgren P, Horányi A, Muñoz Sabater
616 J, Nicolas J, Radu R, Schepers D, Simmons A, Soci C, Thépaut
617 JN (2020) ERA5 monthly averaged data on pressure levels from
618 1950 to 1978 (preliminary version). Copernicus Climate Change Ser-
619 vice (C3S) Climate Data Store (CDS) (Accessed on <19-02-2021>),
620 [https://cds.climate.copernicus.eu/cdsapp#!/dataset/reanalysis-era5-
621 pressure-levels-monthly-means-preliminary-back-extension?tab=overview](https://cds.climate.copernicus.eu/cdsapp#!/dataset/reanalysis-era5-pressure-levels-monthly-means-preliminary-back-extension?tab=overview)
- 622 Benjamini Y, Hochberg Y (1995) Controlling the False Discovery Rate: A
623 Practical and Powerful Approach to Multiple Testing. *Journal of the Royal
624 Statistical Society: Series B (Methodological)* 57(1):289–300, DOI 10.1111/j.2517-6161.1995.tb02031.x
- 626 Cai W, Watterson IG (2002) Modes of Interannual Variability of the South-
627 ern Hemisphere Circulation Simulated by the CSIRO Climate Model. *Jour-
628 nal of Climate* 15(10):1159–1174, DOI 10.1175/1520-0442(2002)015<1159:
629 MOIVOT>2.0.CO;2
- 630 Cai W, van Rensch P, Cowan T, Hendon HH (2011) Teleconnection Pathways
631 of ENSO and the IOD and the Mechanisms for Impacts on Australian Rain-
632 fall. *Journal of Climate* 24(15):3910–3923, DOI 10.1175/2011JCLI4129.1
- 633 Cai W, McPhaden MJ, Grimm AM, Rodrigues RR, Taschetto AS, Garreaud
634 RD, Dewitte B, Poveda G, Ham YG, Santoso A, Ng B, Anderson W, Wang
635 G, Geng T, Jo HS, Marengo JA, Alves LM, Osman M, Li S, Wu L, Karam-
636 peridou C, Takahashi K, Vera C (2020) Climate impacts of the El Niño–
637 Southern Oscillation on South America. *Nature Reviews Earth & Environ-
638 ment* 1(4):215–231, DOI 10.1038/s43017-020-0040-3
- 639 Campitelli E (2020) metR: Tools for Easier Analysis of Meteorological Fields
- 640 Campitelli E, Díaz LB, Vera C (2021) Assessment of zonally symmetric and
641 asymmetric components of the Southern Annular Mode using a novel ap-
642 proach. *Clim Dyn* DOI 10.1007/s00382-021-05896-5
- 643 Dowle M, Srinivasan A (2020) Data.table: Extension of 'data.frame'
- 644 Fogt RL, Marshall GJ (2020) The Southern Annular Mode: Variability, trends,
645 and climate impacts across the Southern Hemisphere. *WIREs Climate
646 Change* 11(4):e652, DOI 10.1002/wcc.652
- 647 Gong D, Wang S (1999) Definition of Antarctic Oscillation index. *Geophysical
648 Research Letters* 26(4):459–462, DOI 10.1029/1999GL900003
- 649 Grytsai A (2011) Planetary wave peculiarities in Antarctic ozone distribution
650 during 1979–2008. *International Journal of Remote Sensing* 32(11):3139–

- 651 3151, DOI 10.1080/01431161.2010.541518
- 652 Hartmann DL, Garcia RR (1979) A Mechanistic Model of Ozone Transport
653 by Planetary Waves in the Stratosphere. *Journal of the Atmospheric Sci-
654 ences* 36(2):350–364, DOI 10.1175/1520-0469(1979)036<0350:AMMOOT>
655 2.0.CO;2
- 656 Hersbach H, Bell B, Berrisford P, Biavati G, Horányi A, Muñoz Sabater J,
657 Nicolas J, Peubey C, Radu R, Rozum I, Schepers D, Simmons A, Soci C, Dee
658 D, Thépaut JN (2019) ERA5 monthly averaged data on pressure levels from
659 1979 to present. Copernicus Climate Change Service (C3S) Climate Data
660 Store (CDS) (Accessed on <08-03-2021>), DOI 10.24381/cds.6860a573
- 661 Hobbs WR, Raphael MN (2010) Characterizing the zonally asymmetric com-
662 ponent of the SH circulation. *Clim Dyn* 35(5):859–873, DOI 10.1007/s00382-
663 009-0663-z
- 664 Horel JD (1984) Complex Principal Component Analysis: Theory and Exam-
665 ples. *Journal of Applied Meteorology and Climatology* 23(12):1660–1673,
666 DOI 10.1175/1520-0450(1984)023<1660:CPCATA>2.0.CO;2
- 667 Huang B, Thorne PW, Banzon VF, Boyer T, Chepurin G, Lawrimore JH,
668 Menne MJ, Smith TM, Vose RS, Zhang HM (2017) Extended Reconstructed
669 Sea Surface Temperature, Version 5 (ERSSTv5): Upgrades, Validations, and
670 Intercomparisons. *Journal of Climate* 30(20):8179–8205, DOI 10.1175/JCLI-
671 D-16-0836.1
- 672 Hufkens K (2020) Ecmwfr: Programmatic interface to the two European Cen-
673 tre for Medium-Range Weather Forecasts API services
- 674 Irving D, Simmonds I (2015) A Novel Approach to Diagnosing Southern
675 Hemisphere Planetary Wave Activity and Its Influence on Regional Climate
676 Variability. *Journal of Climate* 28(23):9041–9057, DOI 10.1175/JCLI-D-15-
677 0287.1
- 678 Irving D, Simmonds I (2016) A New Method for Identifying the Pacific–South
679 American Pattern and Its Influence on Regional Climate Variability. *Journal of Climate*
680 29(17):6109–6125, DOI 10.1175/JCLI-D-15-0843.1
- 681 Katz RW, Brown BG (1991) The problem of multiplicity in research on
682 teleconnections. *International Journal of Climatology* 11(5):505–513, DOI
683 10.1002/joc.3370110504
- 684 Marshall GJ (2003) Trends in the Southern Annular Mode from Observations
685 and Reanalyses. *J Climate* 16(24):4134–4143, DOI 10.1175/1520-0442(2003)
686 016<4134:TITSAM>2.0.CO;2
- 687 Mo KC (2000) Relationships between Low-Frequency Variability in the South-
688 ern Hemisphere and Sea Surface Temperature Anomalies. *Journal of Cli-
689 mate* 13(20):3599–3610, DOI 10.1175/1520-0442(2000)013<3599:RBLFVI>
690 2.0.CO;2
- 691 Mo KC, Paegle JN (2001) The Pacific–South American modes and their down-
692 stream effects. *International Journal of Climatology* 21(10):1211–1229, DOI
693 10.1002/joc.685
- 694 Plumb RA (1985) On the Three-Dimensional Propagation of Stationary
695 Waves. *J Atmos Sci* 42(3):217–229, DOI 10.1175/1520-0469(1985)042<0217:
696 OTTDPO>2.0.CO;2

- 697 R Core Team (2020) R: A Language and Environment for Statistical Comput-
698 ing. R Foundation for Statistical Computing, Vienna, Austria
- 699 Raphael M (2003) Recent, Large-Scale Changes in the Extratropical Southern
700 Hemisphere Atmospheric Circulation. *J Climate* 16(17):2915–2924, DOI
701 10.1175/1520-0442(2003)016<2915:RLCITE>2.0.CO;2
- 702 Raphael MN (2004) A zonal wave 3 index for the Southern Hemisphere. *Geo-*
703 *physical Research Letters* 31(23), DOI 10.1029/2004GL020365
- 704 Raphael MN (2007) The influence of atmospheric zonal wave three on
705 Antarctic sea ice variability. *Journal of Geophysical Research: Atmospheres*
706 112(D12), DOI 10.1029/2006JD007852
- 707 Smith AK (1995) Numerical simulation of global variations of temperature,
708 ozone, and trace species in the stratosphere. *Journal of Geophysical Re-*
709 *search: Atmospheres* 100(D1):1253–1269, DOI 10.1029/94JD02395
- 710 Trenberth KE (1980) Planetary Waves at 500 mb in the Southern Hemisphere.
711 *Mon Wea Rev* 108(9):1378–1389, DOI 10.1175/1520-0493(1980)108<1378:
712 PWAMIT>2.0.CO;2
- 713 Trenberth KF, Mo KC (1985) Blocking in the Southern Hemisphere. *Mon Wea*
714 *Rev* 113(1):3–21, DOI 10.1175/1520-0493(1985)113<0003:BITSH>2.0.CO;
715 2
- 716 Turner J, Hosking JS, Bracegirdle TJ, Phillips T, Marshall GJ (2017) Variabil-
717 ity and trends in the Southern Hemisphere high latitude, quasi-stationary
718 planetary waves. *International Journal of Climatology* 37(5):2325–2336,
719 DOI 10.1002/joc.4848
- 720 van Loon H, Jenne RL (1972) The zonal harmonic standing waves in the
721 southern hemisphere. *Journal of Geophysical Research* 77(6):992–1003, DOI
722 10.1029/JC077i006p00992
- 723 Walker SGT (1914) Correlation in Seasonal Variations of Weather, III: On the
724 Criterion for the Reality of Relationships Or Periodicities. Meteorological
725 Office
- 726 Wickham H (2009) Ggplot2: Elegant Graphics for Data Analysis. Use R!,
727 Springer-Verlag, New York, DOI 10.1007/978-0-387-98141-3
- 728 Wilks D (2011) Statistical Methods in the Atmospheric Sciences, vol 100.
729 Elsevier, DOI 10.1016/B978-0-12-385022-5.00022-1
- 730 Wilks DS (2016) “The Stippling Shows Statistically Significant Grid Points”:
731 How Research Results are Routinely Overstated and Overinterpreted, and
732 What to Do about It. *Bull Amer Meteor Soc* 97(12):2263–2273, DOI 10.
733 1175/BAMS-D-15-00267.1
- 734 Wirth V (1993) Quasi-stationary planetary waves in total ozone and their
735 correlation with lower stratospheric temperature. *Journal of Geophysical*
736 *Research: Atmospheres* 98(D5):8873–8882, DOI 10.1029/92JD02820
- 737 Xie P, Arkin PA (1997) Global Precipitation: A 17-Year Monthly Analysis
738 Based on Gauge Observations, Satellite Estimates, and Numerical Model
739 Outputs. *Bull Amer Meteor Soc* 78(11):2539–2558, DOI 10.1175/1520-
740 0477(1997)078<2539:GPAYMA>2.0.CO;2
- 741 Xie Y (2015) Dynamic Documents with R and Knitr, 2nd edn. Chapman and
742 Hall/CRC, Boca Raton, Florida